photonics

MDPI

Article

Process Research of Surface Laser Phase Transformation Hardening for 42CrMo Material

Peiyu He [1,2,*], Yi Ding [2], Xinyao Hu [2], Liming Qian [1], Yun Wang [1,2] and Fuzhu Li [1,2]

[1] School of Mechanical Engineering, Nantong Institute of Technology, Nantong 226001, China
[2] School of Mechanical Engineering, Jiangsu University, Zhenjiang 212013, China
* Correspondence: hepeiyu@ujs.edu.cn

Abstract: 42CrMo is an ultra-high-strength, low-alloy structural steel. To enhance its surface wear resistance and prolong the service life of components, surface strengthening techniques are commonly applied. In this study, a numerical model for the laser phase transformation hardening of 42CrMo was established. The temperature field and metallurgical transformations during the laser phase transformation hardening process were investigated through numerical simulation, and the morphology of the hardened layer after laser surface treatment was predicted. The effects of key process parameters on the temperature field and the characteristics of the hardened layer were identified. The optimal parameters for single-pass laser phase transformation hardening were found to be a laser power of 1200 W, a scanning speed of 20 mm/s, and a spot diameter of 6 mm. The accuracy of the simulation results was validated through laser phase transformation hardening experiments. The results indicate that under these optimal conditions—laser power of 1200 W and a scanning speed of 20 mm/s—the hardening effect is maximized. The surface hardness reaches a maximum of 782 $HV_{0.2}$, with a cross-sectional hardness peaking at 875 $HV_{0.2}$, which is three to four times higher than the base material's hardness, with an average surface hardness of 745 $HV_{0.2}$.

Keywords: 42CrMo; laser phase transformation hardening; numerical simulation; processing technology; optimization design

check for updates

Citation: He, P.; Ding, Y.; Hu, X.; Qian, L.; Wang, Y.; Li, F. Process Research of Surface Laser Phase Transformation Hardening for 42CrMo Material. *Photonics* **2024**, *11*, 1205. https://doi.org/10.3390/photonics11121205

Received: 5 November 2024
Revised: 21 November 2024
Accepted: 20 December 2024
Published: 22 December 2024

1. Introduction

42CrMo is a high-quality alloy structural steel, commonly used for manufacturing components that require exceptional strength, toughness, and wear resistance. This material is widely applied in mechanical engineering, automotive manufacturing, aerospace, and other fields. Laser phase transformation hardening is a surface treatment process that employs a high-energy-density laser beam to rapidly heat and cool the material's surface. The process leverages the effects of rapid heating and cooling on the material's microstructure [1–3]. Experimental results have shown that laser phase transformation hardening produces a hardened layer structure superior to that of traditional phase transformation hardening methods [4–6]. The surface hardness and wear resistance achieved through this technique surpass those obtained via conventional surface treatments while maintaining the workpiece's plasticity, toughness, and dimensional integrity [7–11].

Laser quenching represents an advanced heat treatment technology, and significant research has been conducted through both experimental and numerical simulations on the laser quenching of steel. Muthukumaran et al. [12] performed laser phase transformation hardening experiments on steel surfaces using various types of lasers. By adjusting factors such as laser wavelength, power intensity, scanning speed, defocusing amount, the surrounding environment, surface pre-treatment, and surface absorptivity, they examined the effects of these parameters on the outcomes of surface hardening. Their findings indicated that the hardness of the hardened layer after single-pass laser phase transformation hardening could reach three to four times that of the substrate. However, in multi-pass

overlap areas, hardness values were reduced by 100 to 400 HV compared to single-pass regions. Maharjan et al. [13] utilized a ytterbium-doped fiber laser for direct gas-assisted laser hardening of AISI 1020 steel in four controlled gas environments, with gas type being the only variable. Their results demonstrated that laser phase transformation hardening under propane produced a hardened layer with a surface hardness significantly higher than that achieved through traditional laser hardening processes, thereby confirming that controlled gas environments can modify the surface properties of steel during laser hardening. Li et al. [14] employed the CALPHAD method to calculate the thermal physical parameters of materials and developed a numerical model for the laser phase transformation hardening process of 40Cr gear steel. There are a number of challenges in the laser phase change hardening process, including uneven thickness of the hardened layer, incomplete phase change, and tempering softening in the lap region of multi-lap laser phase change hardening, which directly affect the quality of the hardening. The current primary method of obtaining laser phase change hardening process parameters is through experimentation. Due to the short duration of the laser surface phase change hardening process, the temperature changes dramatically, and it is difficult to use the experimental method to directly observe or obtain the temperature field during the process, which is inconvenient for the study of the mechanism.

The aforementioned studies confirm that laser phase transformation hardening enhances the surface hardness and wear resistance of 42CrMo. This paper builds on these findings by analyzing the impact of variations in laser process parameters on the quality of the hardened layer through numerical simulations of the temperature field and microstructure distribution. Experimental validation of the simulation results was carried out, confirming the observed influence patterns. This research enables the efficient prediction of optimal process parameters via simulation, significantly reducing experimental time and costs. Furthermore, it provides a theoretical foundation for refining laser processing parameters based on a more profound understanding of laser surface treatment effects.

2. Modeling and Experimental Setup of Laser Phase Transformation Hardening for 42CrMo

2.1. Modeling of Laser Phase Transformation Hardening for 42CrMo

42CrMo steel exhibits excellent hardness and toughness, with its chemical composition provided in Table 1. The samples used for this study were hot-rolled 42CrMo round steel, with dimensions of 120 mm × 80 mm × 15 mm, as shown in Figure 1a. Before undergoing laser phase transformation hardening, the sample surfaces were ground and cleaned with anhydrous ethanol to prevent local energy discrepancies during the hardening process, ensuring uniform hardening results. Additionally, an absorbent coating was applied to the sample surfaces prior to laser processing, as illustrated in Figure 1b. Pre-simulation and experimental comparisons revealed that the absorption rate of the samples increased to approximately 91% after the application of the absorbent coating. The primary elemental composition of the samples is detailed in Table 1. The laser phase transformation hardening experiments were conducted using a GLS.IB type 3000 W multifunctional CO_2 laser processing system, as shown in Figure 1c. The laser beam formed a circular spot with a diameter of 6 mm, featuring an energy distribution that approximated a Gaussian profile. During the simulation, the specimen size was reduced to 35 mm × 30 mm × 10 mm, as depicted in Figure 1d. In the figure, the orange section represents a schematic model of the Gaussian 2D laser heat source, with the red arrow indicating the direction of the laser spot movement. The yellow dashed box delineates the heat-affected zone, which was defined in the simulation software to exclusively receive the heat source's influence. The bottom surface of the specimen was fixed, and all external surfaces were designated as cooling surfaces.

Table 1. Main chemical components of 42CrMo (Wt%).

Element	C	Si	Mn	Cr	Ni	Mo	V
Component	0.38~0.45	0.17~0.37	0.5~0.8	0.9~1.2	0.08	0.15~0.29	0.01

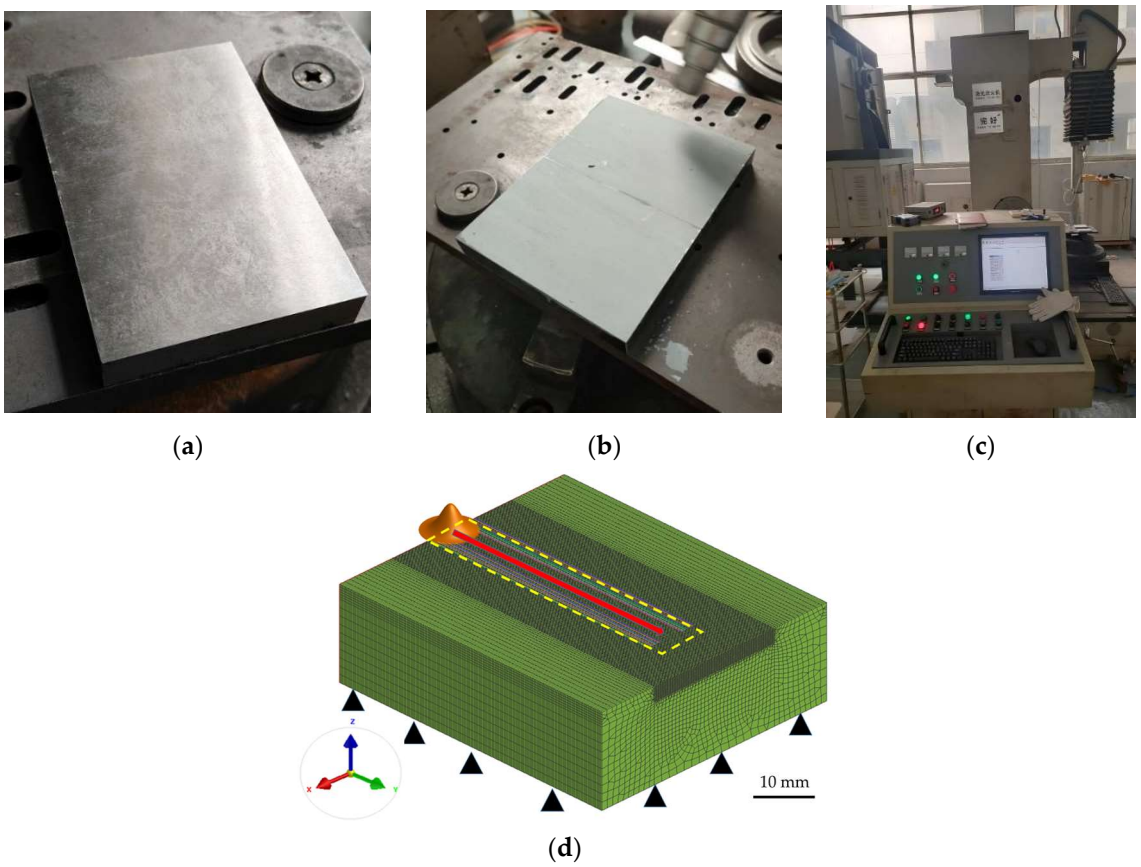

Figure 1. (**a**) Original sample; (**b**) Surface-coated sample; (**c**) Laser processing system; (**d**) Laser phase transformation hardening model of shield main bearing.

The temperature field and microstructural evolution during the laser quenching process were simulated using SYSWELD 2019 software, with an analysis of temperature and microstructural changes. In the simulation process, the heat conduction differential Equation (1) was employed:

$$\frac{\partial}{\partial x}\left(\lambda\frac{\partial T}{\partial x}\right)+\frac{\partial}{\partial y}(\lambda\frac{\partial T}{\partial y})+\frac{\partial}{\partial z}\left(\lambda\frac{\partial T}{\partial z}\right)+Q(x,y,z,t)=\rho C_p\frac{\partial T}{\partial t} \quad (1)$$

where x, y, z is the three-dimensional coordinate, C_p is the specific heat capacity, $Q(x,y,z,t)$ is the latent heat of phase change, ρ is the material density, λ is the thermal conductivity, T is the temperature distribution function. Boundary conditions were specified by Equation (2):

$$\lambda\left(\frac{\partial T}{\partial x}n_x+\frac{\partial T}{\partial y}n_y+\frac{\partial T}{\partial z}n_z\right)=\alpha(T-T_0) \quad (2)$$

where n_x, n_y, n_z are direction cosines in the x, y, z directions, T_0 is ambient temperature, α is composite heat transfer coefficient. The ambient temperature T_0 is set as a constant

20 °C. The region heated by scanning the laser spot on the workpiece can be considered as an additional heat flux density term, expressed by Equation (3):

$$\lambda\left(\frac{\partial T}{\partial x}n_x + \frac{\partial T}{\partial y}n_y + \frac{\partial T}{\partial z}n_z\right) = q_s(x, y, z, t) \tag{3}$$

where q_s represents the external heat flux per unit area. The final input power is given by Equation (4):

$$P = P_0 \cdot \eta = v \cdot H \cdot \eta \tag{4}$$

where P represents the final absorbed power, P_0 is the laser input power, H is the line energy density, v is the scanning speed, η is the heat absorption rate.

Laser energy density describes the energy distribution of a laser beam over a scanned area and is defined by the Equation (5):

$$E = \frac{P_0 \times t}{S} = \frac{P_0}{d \times v} \tag{5}$$

where E is laser energy density, S is laser spot scanning area, d is laser spot diameter, mm.

2.2. Laser Phase Transformation Process Parameters and Experiments

In this study, adjustments were made to the laser power and scanning speed, and the depth of the hardened layer in specimens subjected to the same laser energy density was compared. The specific laser processing parameters are provided in Table 2. Additionally, several control simulation groups were included in the numerical simulations. Both the numerical simulations and experimental procedures were conducted at room temperature. The microstructures of the laser-quenched specimen cross-sections, after cold embedding, were analyzed using a Zeiss AX.10 metallographic microscope (Zeiss, Jena, Germany) and a Zeiss EVO.18 tungsten filament scanning electron microscope (Zeiss, Jena, Germany). Microhardness measurements were performed using the Vision Microhardness Tester (HXD.1000TMSC/LCD)(Shanghai Optical Instruments Import & Export Co., Shanghai, China) with a 0.2 kg load, assessing hardness both in the surface width direction and the cross-sectional depth direction of the hardened layer.

Table 2. Laser brazing parameters.

Serial Number	Power (W)	Scanning Rate (mm/s)	Laser Energy Density (J/mm^2)
1	800	20	6.67
2	1000	20	8.33
3	1200	20	10
4	1400	20	11.67
5	1200	10	20
6	1200	12	16.67
7	1200	15	13.33
8	1200	24	8.33
9	1400	28	8.33
10	1600	32	8.33

3. Results and Discussion

3.1. Simulation Results

Figure 2a presents the temperature variation curves at node 337,259, located in the middle of the specimen, for scanning speeds of 20 mm/s and laser powers of 600 W, 800 W, 1000 W, 1200 W, and 1400 W. From the temperature changes depicted in the figure, it is evident that, at a constant laser scanning speed, the maximum temperature on the shield machine's main bearing raceway surface increases with rising laser power. The duration within the high-temperature range also slightly increases, along with the heating and cooling rates. When the laser scanning speed is 20 mm/s and the laser power is 1400 W,

the maximum temperature on the shield machine's main bearing raceway surface reaches 1626.9 °C, which exceeds the melting temperature, 1400 °C, of 42CrMo steel [15]. This indicates that, under a constant laser scanning speed, the surface temperature of the specimen increases with rising laser power until it surpasses the melting point. Additionally, the area of the specimen's surface where the temperature exceeds the Ac_1 (lower transformation temperature) and Ac_3 (upper transformation temperature) gradually expands, leading to an increase in both the width of the phase transformation hardening zone and the depth of the hardened layer. However, it is crucial to note that, near the critical point of laser power, slight surface melting of the material may occur, which should be avoided on the surface of the bearing raceway.

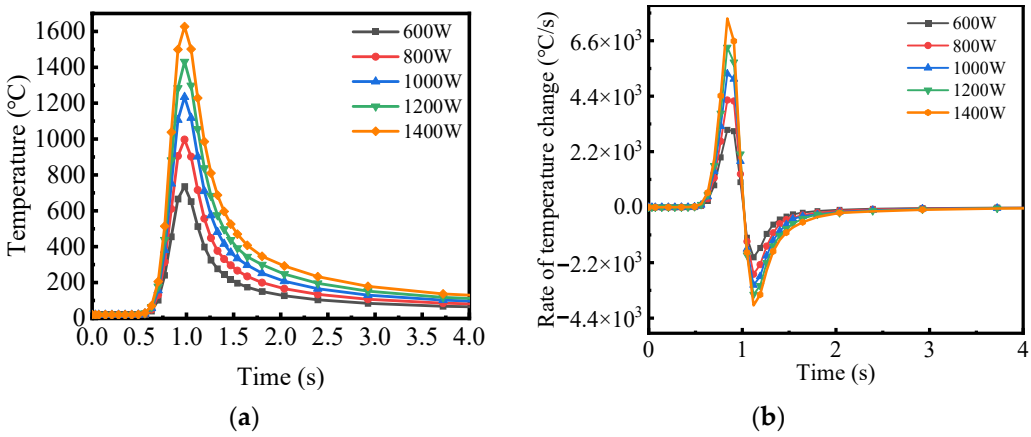

Figure 2. (**a**) Sample surface center temperature curve; (**b**) Sample surface temperature change rate.

The temperature change rate at node 337,259 under different laser powers is depicted in Figure 2b. It can be observed that, at a constant laser scanning speed, higher laser power results in a faster temperature change rate. A higher temperature change rate promotes rapid cooling of the material, which accelerates the formation of austenite and its subsequent transformation into martensite. This leads to the development of finer grains and a greater quantity of martensite, thereby enhancing the material's hardness and strength. Conversely, if the temperature change rate is too slow, it may result in larger grain growth and an uneven microstructure, reducing the effectiveness of the hardening process. Additionally, a faster temperature change rate can minimize material deformation during phase transformation hardening, leading to improved dimensional control and shape retention. However, it is important to note that rapid cooling may also induce higher residual stresses. Therefore, controlling the temperature change rate is crucial for optimizing the effectiveness of laser phase transformation hardening.

Figure 3 illustrates the maximum temperature on the surface, along with the hardened layer depth and hardness, under various laser powers. The numerical simulation employed a two-dimensional Gaussian plane heat source, which is unsuitable for scenarios involving surface melting. As a result, the simulation data for the 1400 W power level exhibit significant discrepancies when compared to actual conditions. Consequently, the simulation results for this power group are marked in red and deemed unreliable. At a laser power of 800 W, the maximum temperature on the shield machine's main bearing raceway surface reaches 997.2 °C, which corresponds to the Ac_3 temperature of 42CrMo steel. In this condition, within a 1.9 mm diameter surrounding the center of the laser spot, the temperature surpasses the Ac_3 point, indicating extensive austenitization in this region. However, the measured width of the hardened layer is only 3.27 mm, with a depth of 0.48 mm, which is insufficient to meet the requirements for effective laser phase transformation hardening. When the laser power is reduced to 600 W, the maximum temperature on the surface of the specimen drops to 736 °C, which is close to the Ac_1 temperature of the

material. As a result, no martensitic transformation occurs on the surface, and a hardened layer formed by phase transformation is not achieved.

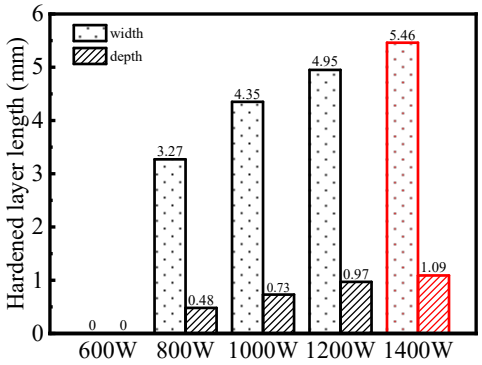

Figure 3. Specimen hardening layer width and depth.

Figure 4a,b present the temperature variations in different specimens at scanning speeds of 10, 20, 30, 40, and 50 mm/s under a constant laser power of 1200 W. As the scanning speed increases, the peak surface temperature of the specimen decreases, along with a reduction in the duration of the high-temperature zone, while both the heating and cooling rates rise. This is primarily because, at constant power, increasing the scanning speed reduces the duration of laser exposure on any given surface area of the specimen, thereby decreasing the total laser energy absorbed by the surface and lowering the peak temperature. However, as the scanning speed increases, the laser energy is delivered to the surface more rapidly, leading to higher rates of temperature change. Additionally, as the temperature decreases, the thermal conductivity of the material increases within the simulated temperature range, further contributing to the increased heating and cooling rates at higher scanning speeds. Under constant power, a faster scanning speed reduces the heat input into the substrate, thereby limiting the area in which the material surface can reach austenitizing temperatures, resulting in narrower and shallower hardened layers.

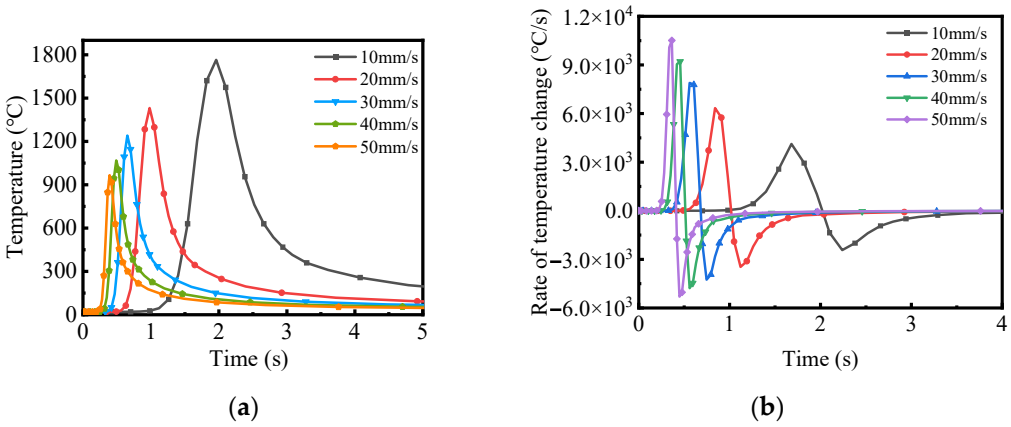

Figure 4. (**a**) Temperature variation curve; (**b**) Rate of temperature change.

For the 1200 W group, where the peak surface temperature remained below the melting point but produced a relatively deep hardened layer, the surface phase volume fraction change curves for each phase were collected and plotted, as shown in Figure 5. Sampling was conducted on cell 449,068, near node 337,259. From 0 to 0.77 s, the heat source had not yet reached this point, and the microstructure of the base metal remained unchanged, containing only the initial phase. At 0.84 s, the temperature exceeded the lower transformation temperature, Ac_1, leading to a rapid decline in the volume fraction of the initial phase as the temperature rose. Concurrently, the austenite volume fraction

increased sharply until 0.91 s, at which point the initial phase had completely transformed into austenite. At 0.98 s, the temperature peaked at 1431.3 °C, with the austenite volume fraction reaching its maximum of 99.9%. Thereafter, as the temperature decreased to around 350 °C at 1.64 s, the austenite volume fraction began to rapidly decrease while the martensite volume fraction increased continuously. By the end of the simulation, at 150 s, the austenite volume fraction had diminished to 4.9%, while the martensite volume fraction had risen to 94.9%. At this stage, the temperature had dropped to 48.2 °C, and the microstructure of the cell predominantly consisted of martensite, with small amounts of retained austenite and trace quantities of residual ferrite and bainite. Laser phase hardening increases the heating rate, the austenite phase transformation is completed in a very short time in the high temperature region with a large degree of superheat, and the cooling rate is much faster than the critical cooling rate of the martensitic phase transformation. The Austenite nucleation rate is very high, with austenite grain refinement. At the same time, the rapid cooling after instantaneous heating means that it is too late for the ultrafine austenite grains to grow, as well as being too late for the carbon atoms to diffuse. With the transformation of austenite to martensite (and if the cooling rate is sufficient to exceed the critical cooling rate of the transformation to martensite), the martensite is very fine. Due to the extremely fast cooling rate, the carbon atoms do not have time to diffuse, resulting in a very high carbon content in the martensite, while the residual austenite also obtains a very high dislocation density.

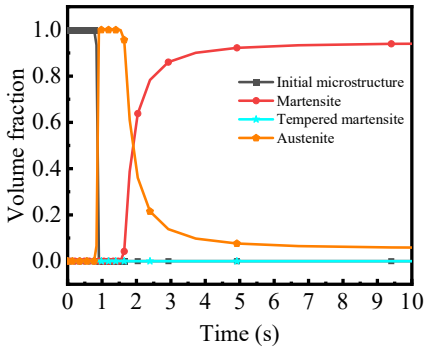

Figure 5. Metallographic volume fraction change.

At the same laser energy density, variations in process parameters result in different widths and depths of the hardened layer. For an energy density of 8.33 J/mm^2, the study simulated the effects of different process parameters on surface temperature and the formation of the hardened layer. Four sets of process parameters, all under the same laser energy density, are presented in Table 3. In these scenarios, increasing the laser power is coupled with an increase in laser scanning speed.

Table 3. Laser brazing parameters.

Serial Number	Power (W)	Scanning Rate (mm/s)	Laser Energy Density (J/mm^2)
1	1000	20	8.33
2	1200	24	
3	1400	28	
4	1600	32	

The graphs in Figure 6a,b present simulation results for four different process parameters under the same laser energy density. From the temperature variations at node 337,259 across these four sets of parameters, it can be observed that, although the laser energy density on the surface of the test piece remains constant, the peak temperature at node 337,259 increases with higher laser power and scanning speed. This suggests that maintaining the same laser energy density does not guarantee a uniform temperature

distribution on the workpiece surface; instead, this is influenced by factors such as laser power and scanning speed. Therefore, when determining the process parameters for laser phase transformation hardening, it is crucial to consider not only the laser energy density but also laser power and scanning speed, to achieve the desired temperature distribution and hardening effect.

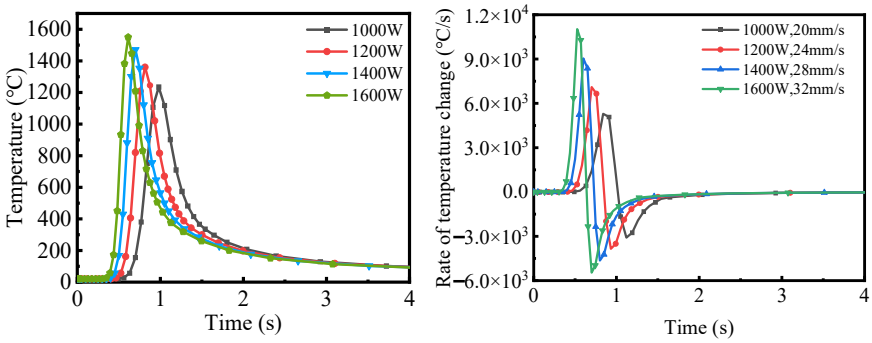

Figure 6. (**a**) Temperature variation curve; (**b**) Rate of temperature change.

Faster scanning speeds result in the rapid transfer of laser energy to the material surface, leading to variations in temperature gradients. When the scanning speed reaches 40 mm/s, noticeable fluctuations in the temperature gradient occur, as evidenced by the wave-like ripples on the hardened surface layer shown in Figure 7a. These ripples appear when the laser scanning speed is too high. Conversely, when the scanning speed is too slow, the laser beam dwells on the specimen surface for an extended period, causing the surface temperature to rise excessively. This can lead to micro-melting, severe burning, or unwanted structural changes. Therefore, to enhance processing efficiency while maintaining a consistent beam size, it is essential to increase the laser power in conjunction with higher scanning speeds. This ensures sufficient heating to raise the specimen surface temperature above the Ac_3 point, thereby balancing the heating duration and temperature gradients to achieve the desired hardening effect.

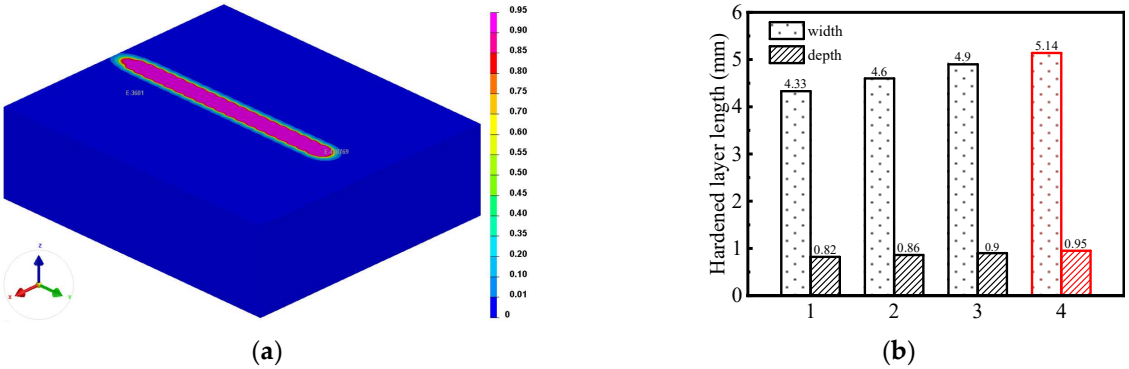

Figure 7. (**a**) Surface morphology of hardened layer is 1200 W, 40 mm/s; (**b**) Specimen hardening layer width and depth.

The width and depth of the hardened layer under four different process parameters are presented in Figure 7b. It can be observed that both the width and depth of the hardened layer correlate positively with the highest surface temperature of the specimen. As the surface temperature and temperature change rate increase, the width and depth of the hardened layer also show a significant increase. However, when the laser power reaches a certain threshold, such as in the fourth group with 1600 W and a scanning speed of 32 mm/s, the highest surface temperature exceeds the material's melting point. In such

cases, the measurements for the width and depth of the hardened layer become unreliable. Consequently, the data for this group are highlighted in red and are not considered valid.

In general, at lower power levels and scanning speeds, the laser remains for longer over the same area, allowing the self-cooling effect of the substrate to control the cooling process during laser phase transformation hardening. This prolonged exposure results in a slower surface temperature change rate, which can lead to the formation of martensite in the microstructure due to carbon diffusion, thereby reducing the surface hardness. Conversely, increasing laser power and scanning speed boosts energy input and the cooling rate per unit time, thereby enhancing the phase transformation hardening effect and improving material hardness. However, rapid heating and cooling processes may introduce significant thermal stresses into the material, potentially compromising its stability and performance. Therefore, careful control of these parameters is crucial to achieve the optimal hardening effect.

3.2. Comparison Between Simulation and Experimental Results

A single-pass laser quenching experiment was conducted using the process parameters outlined in Table 2, and the surface appearance of the samples is shown in Figure 8. After excluding samples that exhibited surface melting, the final experimental results were compared with the numerical simulation data, as presented in Table 4. The comparison revealed that the difference in hardened layer depth between the numerical simulations and experimental measurements was minimal, with errors remaining within 10% for the samples that did not experience melting. Based on both the surface appearance and the depth of the hardened layer, samples 3 and 9 demonstrated superior hardening effects. Consequently, further analysis was performed on these two samples.

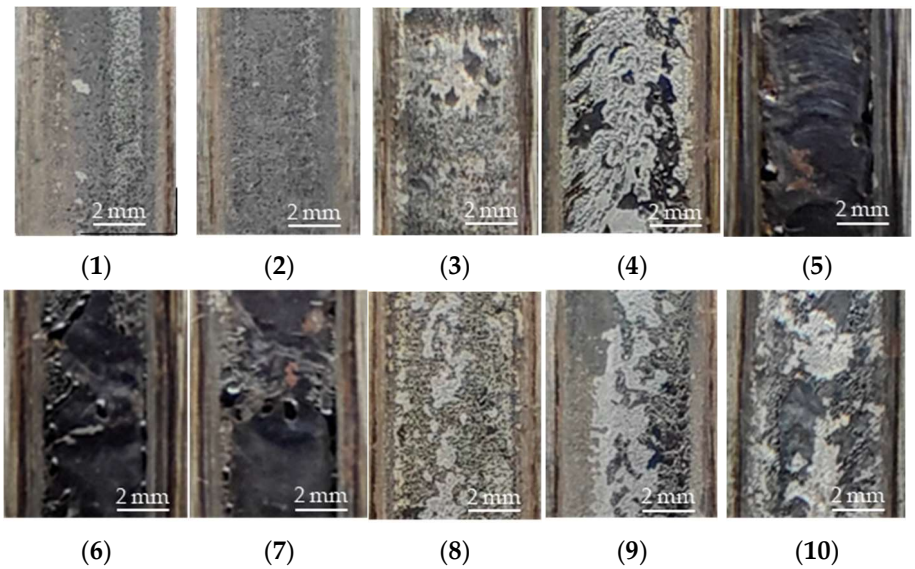

Figure 8. Surface appearance diagram of single-channel laser phase change hardening samples; (**1**)~(**10**) in the figure correspond to samples No. 1~10.

Table 4. Comparison of theoretical solution and finite element solution.

Serial Number	Depth of the Simulation (mm)	Depth of the Test (mm)	Error
1	0.49	0.51	−3.9%
2	0.74	0.80	−7.5%
3	0.88	0.91	−3.3%
8	0.85	0.82	3.7%
9	0.89	0.86	3.5%

3.3. Hardened Layer Cross-Section Profile

The actual cross-sectional morphology of the hardened layer, obtained using process parameters of 1200 W laser power, 20 mm/s scanning speed, and a beam diameter of 6 mm, is shown in Figure 9a. The layer exhibits a crescent-shaped overall appearance. In comparison, Figure 9b presents the martensite content map of the cross-section, generated through simulation using SYSWELD software under the same process parameters. Measurements revealed a 9.2% error in the width of the hardened layer and a 4.6% error in depth between the simulation and the actual results. Both errors are within 10%, indicating a strong agreement between the simulation and experimental outcomes.

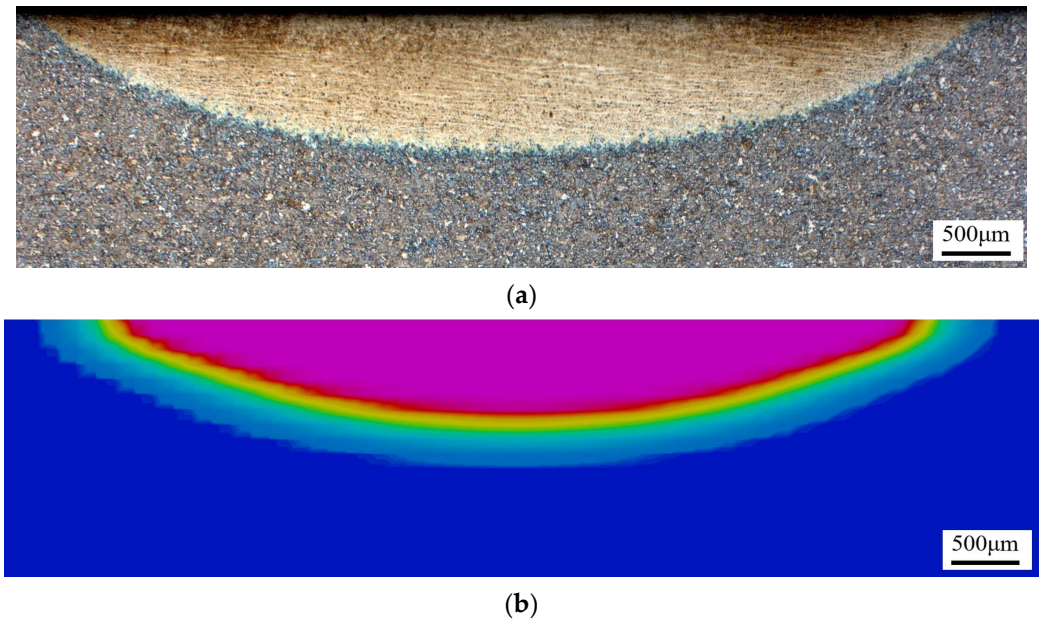

Figure 9. (**a**) Experimental results; (**b**) Simulation results.

3.4. Analysis of Metallographic Structure

The metallographic structure of the hardened layer near the surface center of sample 3, captured using an optical microscope, is shown in Figure 10a. The predominant structures in this region are lath-shaped and needle-shaped martensite. The bright white structures observed between the martensite, lacking a fixed form, are identified as residual austenite. The metallographic morphology at various depths of the sample, obtained under the same process parameters and captured using a scanning electron microscope (SEM), is presented in Figure 10b–d. When the laser beam directly irradiates the material's surface, the surface temperature increases rapidly due to the absorption of laser energy, causing localized heating. This heat is then conducted towards the interior of the material due to its thermal conductivity. However, since the laser's penetration depth is limited, the temperature inside the material remains relatively low. At the same time, the surface cooling rate is relatively slow, due to a slower heat exchange with the surrounding environment, while the interior cools faster because of more efficient thermal conduction. These temperature gradients and uneven cooling rates influence the phase transformations and crystal structure of the material, leading to the formation of complex metallographic structures throughout the hardened layer.

As shown in Figure 10b, the surface temperature of the material is higher, and the cooling rate is slower compared to regions closer to the base material. This prolonged austenitization leads to the formation of coarse martensite structures after cooling, along with a small amount of residual austenite. Figure 10c illustrates the central region of the hardened layer, which, being closer to the base material, experiences faster heating and cooling rates. In this region, austenite transforms into refined martensite structures before

significant growth occurs, resulting in finer martensite compared to the surface. Figure 10d represents the transition zone, which is farther from the surface and undergoes more rapid heat absorption and cooling. The thermal equilibrium temperature in this zone is near the lower critical point, resulting in a mixed structure of base material, martensite, and residual austenite.

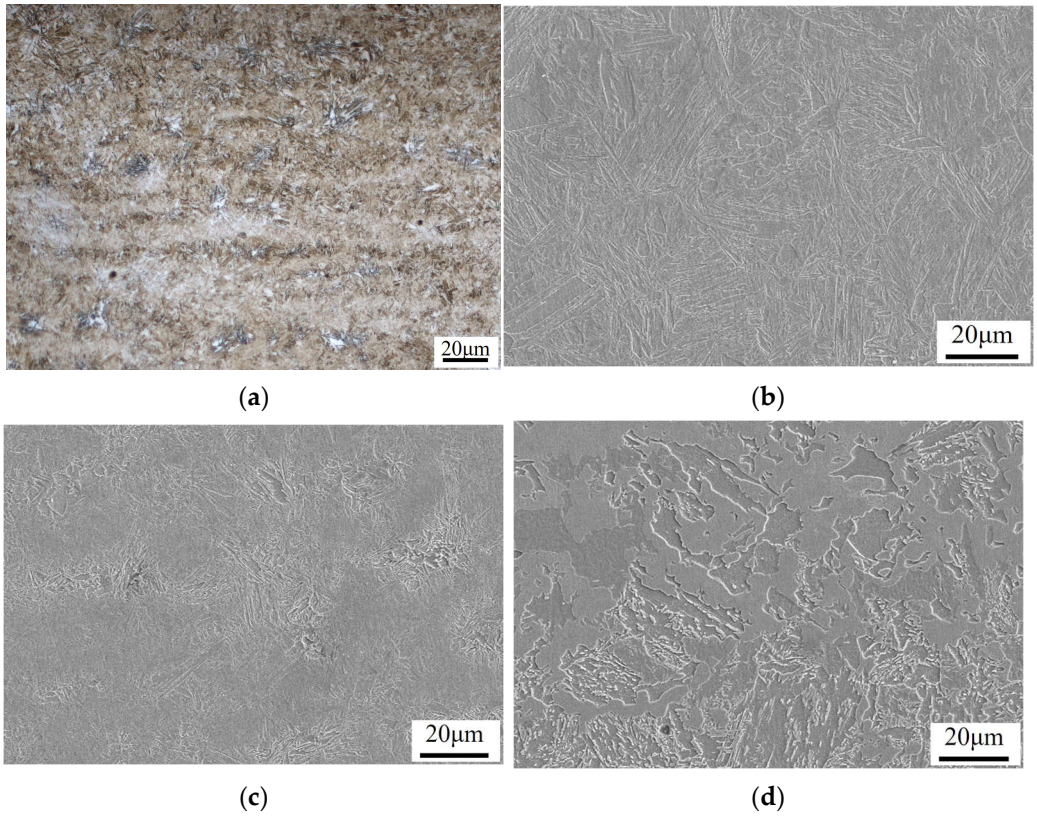

Figure 10. (**a**) Hardening layer morphology of specimen No. 3 cross section; (**b**) Metallographic morphology of top area; (**c**) Metallographic morphology of middle area; (**d**) Metallographic morphology of bottom area.

3.5. Microhardness Analysis

Sections of samples 3 and 9 were selected for hardness testing, starting from the surface toward the substrate at the center of the single-pass laser phase transformation-hardened samples. The Vickers hardness measured along the depth direction is shown in Figure 11a. In sample 3, the hardness at the center region closest to the surface reaches 793.2 $HV_{0.2}$, while the highest hardness within this section is 883.4 $HV_{0.2}$. The microhardness along the depth from the surface toward the substrate shows a slight increase followed by a decrease, with the hardness at 1 mm depth from the surface measuring 243.4 $HV_{0.2}$, which is indicative of the substrate. In contrast, sample 9 exhibits slightly higher surface and subsurface hardness compared to sample 3, with surface hardness reaching 811.8 $HV_{0.2}$ and a hardness of 880.7 $HV_{0.2}$ at a depth of 0.1 mm. The microhardness profile in sample 9 also shows an initial increase followed by a gradual decrease. However, within the hardened layer, the decline in hardness is more gradual, with a pronounced drop occurring at the boundary between the hardened layer and the substrate. This sudden decrease in hardness can be attributed to the high hardness of martensite in the hardened layer, while the substrate, having undergone less heat exposure, experiences minimal or no martensite formation during the laser processing, leading to an abrupt transition in hardness. As highlighted in the previous microstructural analysis, the surface exhibits slightly coarse martensite, while the subsurface and central regions of the hardened layer predominantly consist of fine martensite. The presence of fine martensite introduces more interfaces and

dislocations in the material, which impede dislocation movement, thereby increasing the material's strength and hardness. Consequently, the hardness trend from the surface into the depth shows a slight rise before gradually decreasing. In cross-sectional comparisons, sample 9 shows marginally higher hardness in the surface and subsurface layers, which can be attributed to the increased laser power and scanning speed. These adjustments enhance energy input and cooling rates per unit time, thereby raising the surface hardness. However, this also impacts the uniformity of the phase transformation hardening process, leading to fluctuations in internal hardness. In contrast, sample 3 demonstrates more stable hardness variations, with a better average hardness and greater hardened layer depth.

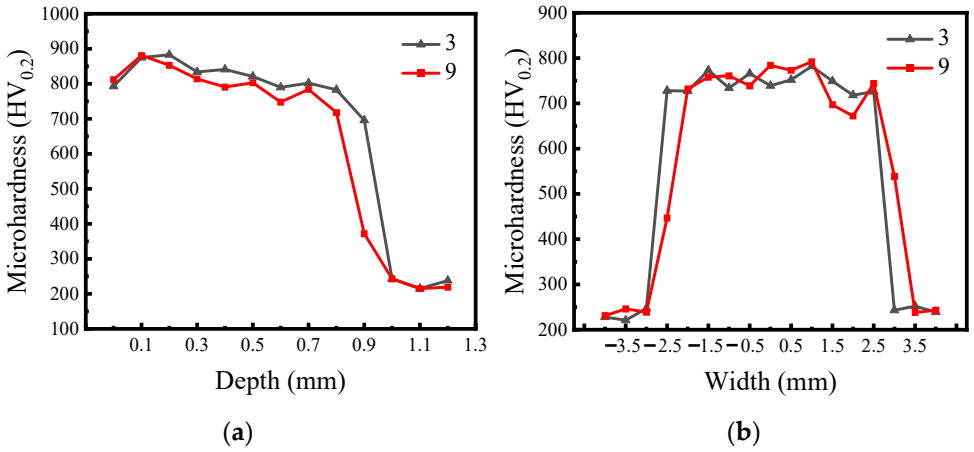

Figure 11. (**a**) Hardness distribution of specimen cross section; (**b**) Sample surface hardness distribution.

The average of the highest three surface hardness points was used as the benchmark for maximum hardness. A value of 75% of this benchmark is considered the threshold for defining the effective hardened layer. The average hardness within this effective hardened layer is recorded as the sample's surface average hardness. Figure 11b presents a line graph illustrating the surface hardness measurements and their distribution, measured from the centerline of the hardened zone toward both sides for samples 3 and 9. For sample 3, the highest surface hardness reaches 782 $HV_{0.2}$, with an average hardness of 744.9 $HV_{0.2}$, and the effective hardened width is approximately 5.4 mm. Sample 9 exhibits a slightly higher surface hardness of 792 $HV_{0.2}$, with an average hardness of 745.2 $HV_{0.2}$, and an effective hardened width of around 5.1 mm. Although sample 9 shows a marginally higher surface average hardness, the difference is not significant. Sample 3, however, has a wider effective hardened layer and a more uniform surface hardness distribution. Based on the comparison of these two laser surface phase transformation hardening experiments, it can be concluded that sample 3 demonstrates better overall performance.

4. Conclusions

This study focuses on the 42CrMo material and applies laser phase transformation hardening for surface strengthening. The conclusions are as follows:

(1) The laser phase transformation hardening process for the surface exhibits rapid heating and cooling characteristics, with temperatures rising and falling sharply during laser exposure, accompanied by extremely fast heating and cooling rates. As laser power increases, surface temperatures rise until exceeding the melting point, with an associated increase in the rate of temperature change. Higher scan speeds result in lower surface temperatures and faster temperature change rates, but excessive scan speeds can negatively impact the uniformity of the hardened layer. Under the same energy density, increasing both power and scan speed leads to higher peak surface temperatures. After evaluating surface temperature and hardened layer depth, it was determined that the process parameters of 1200 W power, 20 mm/s scan speed, and a 6 mm spot size produce the deepest hardened layer of 0.97 mm.

(2) The simulation results confirm that the cross-sectional morphology of the hardened layer from laser phase transformation hardening closely matches the simulated microstructure cross-section. The discrepancy between the simulated hardened layer morphology (in cases where the peak temperature does not reach the melting point) and the experimental results is within 10%. The hardened layer is primarily composed of martensite, with the martensite content gradually decreasing from the surface toward the substrate. Hardness peaks in the subsurface layer and gradually decreases towards the substrate. For example, under 1200 W laser power and a 20 mm/s scan speed, the maximum surface hardness reaches 782 $HV_{0.2}$, while the cross-sectional hardness peaks at 875 $HV_{0.2}$—approximately three to four times higher than the substrate hardness. The average surface hardness is 745 $HV_{0.2}$. The optimal hardening effect is achieved with laser power of 1200 W and a scan speed of 20 mm/s.

Author Contributions: Conceptualization, P.H.; methodology, L.Q.; software, X.H.; validation, P.H.; formal analysis, Y.D.; investigation, F.L.; writing—original draft preparation, Y.D.; writing—review and editing, P.H.; visualization, P.H.; supervision, Y.W.; project administration, P.H.; funding acquisition, P.H. All authors have read and agreed to the published version of the manuscript.

Funding: The authors gratefully acknowledge the support provided by the National Natural Science Foundation of China (No. 52105259), Jiangsu Province Natural Science Foundation (No. BK20220533), Jiangsu Province's "Blue Project" (Su Teacher's Letter [2024] No. 2), and China Postdoctoral Science Foundation (No. 2022M721371).

Institutional Review Board Statement: Not applicable.

Informed Consent Statement: Not applicable.

Data Availability Statement: All datasets generated in this study are available from the corresponding author upon reasonable request.

Conflicts of Interest: The authors declare that there are no conflicts of interest.

References

1. Atabay, S.E.; Sanchez-Mata, O.; Muñiz-Lerma, J.A.; Brochu, M. Effect of heat treatment on the microstructure and elevated temperature tensile properties of Rene 41 alloy produced by laser powder bed fusion. *J. Alloys Compd.* **2020**, *858*, 157645. [CrossRef]
2. Catalán, N.; Ramos-Moore, E.; Boccardo, A.; Celentano, D. Surface Laser Treatment of Cast Irons: A Review. *Metals* **2022**, *12*, 562. [CrossRef]
3. Makarov, A.V.; Korshunov, L.G.; Malygina, I.Y.; Osintseva, A.L. Effect of laser quenching and subsequent heat treatment on the structure and wear resistance of a cemented steel 20KhN3A. *Phys. Met. Met.* **2007**, *103*, 507–518. [CrossRef]
4. Chen, Z.; Zhu, Q.; Wang, J.; Yun, X.; He, B.; Luo, J. Behaviors of 40Cr steel treated by laser quenching on impact abrasive wear. *Opt. Laser Technol.* **2018**, *103*, 118–125. [CrossRef]
5. Zhang, T.; Fan, Q.; Ma, X.; Wang, W.; Wang, K.; Shen, P.; Yang, J. Microstructure and Mechanical Properties of Ti-35Nb-2Ta-3Zr Alloy by Laser Quenching. *Front. Mater.* **2019**, *6*, 318. [CrossRef]
6. Kwok, C.; Wong, P.; Man, H. Enhancement in corrosion and electrical wear resistance of copper via laser surface alloying with NiTi. *Surf. Coat. Technol.* **2021**, *408*, 126804. [CrossRef]
7. Khorram, A.; Jamaloei, A.D.; Jafari, A. Surface transformation hardening of Ti-5Al-2.5Sn alloy by pulsed Nd:YAG laser: An experimental study. *Int. J. Adv. Manuf. Technol.* **2018**, *100*, 3085–3099. [CrossRef]
8. Pan, X.; Zhou, L.; Hu, D.; He, W.; Liu, P.; Yu, Z.; Liang, X. Superior wear resistance in cast aluminum alloy via femtosecond laser induced periodic surface structures and surface hardening layer. *Appl. Surf. Sci.* **2023**, *636*, 157866. [CrossRef]
9. Chen, Z.; Yu, X.; Ding, N.; Cong, J.; Sun, J.; Jia, Q.; Wang, C. Wear resistance enhancement of QT700-2 ductile iron crankshaft processed by laser hardening. *Opt. Laser Technol.* **2023**, *164*, 109519. [CrossRef]
10. Wagh, S.V.; More, S.R.; Madhav, V.V.V.; Saxena, K.K.; Bandhu, D.; Sunil, B.; V, R.; Siddiqui, I.H. Effects of low-power laser hardening on the mechanical and metallurgical properties of biocompatible SAE 420 steel. *J. Mater. Res. Technol.* **2024**, *30*, 1611–1619. [CrossRef]
11. Li, J.; Yan, H.; Li, S.; Lei, M. Microstructure and wear behavior of arc-shaped 40CrNiMo steel after laser hardening. *J. Mater. Res. Technol.* **2023**, *24*, 5743–5754. [CrossRef]
12. Muthukumaran, G.; Babu, P.D. Laser transformation hardening of various steel grades using different laser types. *J. Braz. Soc. Mech. Sci. Eng.* **2021**, *43*, 103. [CrossRef]

13. Maharjan, N.; Zhou, W.; Wu, N. Direct laser hardening of AISI 1020 steel under controlled gas atmosphere. *Surf. Coatings Technol.* **2020**, *385*, 125399. [CrossRef]
14. Li, C.; Gao, H.; Chen, X.; Liu, Z.; Han, X. Study on Multi-Field Coupled Evolution Mechanism of Laser Irradiated 40Cr Steel Quenching Process Based on Phase Change Induced Plasticity. *Met. Mater. Int.* **2021**, *28*, 1919–1937. [CrossRef]
15. He, P.; Ding, Y.; Jiang, S.; Zhang, H.; Shen, T.; Wang, Y. Process Parameters Analysis of Laser Phase Transformation Hardening on the Raceway Surface of Shield Main Bearing. *Photonics* **2023**, *10*, 287. [CrossRef]